Journal of Materials Chemistry C

ROYAL SOCIETY OF CHEMISTRY

PAPER

View Article Online
View Journal | View Issue

Cite this: J. Mater. Chem. C, 2020, 8, 4049

Magnon-drag thermopower in antiferromagnets *versus* ferromagnets†

Md. Mobarak Hossain Polash,[ab] Farzad Mohaddes,[b] Morteza Rasoulianboroujeni[c] and Daryoosh Vashaee*[ab]

Received 19th November 2019,
Accepted 15th January 2020

DOI: 10.1039/c9tc06330g

rsc.li/materials-c

The extension of magnon electron drag (MED) to the paramagnetic domain has recently shown that it can create a thermopower more significant than the classical diffusion thermopower resulting in a thermoelectric figure-of-merit greater than unity. Due to their distinct nature, ferromagnetic (FM) and antiferromagnetic (AFM) magnons interact differently with the carriers and generate different amounts of drag-thermopower. The question arises of whether the MED is stronger in FM or in AFM semiconductors. Two material systems, namely MnSb and CrSb, which are similar in many aspects except that the former is FM and the latter AFM, were studied in detail, and their MED properties were compared. Three features of AFMs compared to FMs, namely double degeneracy of the magnon modes, higher magnon group velocity, and longer magnon relaxation time, can lead to enhanced first-order MED thermopower. One effect, magnon–electron relaxation, leads to a higher second-order effect in AFMs that reduces the MED thermopower. However, it is generally expected that the first-order effect dominates and leads to a higher drag thermopower in AFMs, as seen in this case study.

Introduction

Recently, spin-caloritronic effects in magnetic semiconductors like magnon electron drag (MED),[1,2] paramagnon electron drag[3–6] and spin-entropy[7–9] have shown significant prospects in enhancing the thermoelectric figure-of-merit (zT), and hence the efficiency, by improving the thermoelectric power-factor ($S^2\sigma$), which comprises electrical conductivity (σ) and thermopower or Seebeck coefficient (S). Reciprocal interactions between electrons, phonons, and magnon lead to enhancing the thermopower through the contribution of linearly coupled advective and diffusive transport processes within the crystal.[3,10–12] The contribution of the spin degree of freedom to the thermopower or electrical conductivity can come from both spins of electron residing in the orbital and the collective spins of lattice ions, which can form long-range or short-range spin-waves known as magnons and paramagnons, which are bosonic quasiparticles. Historically, magnon–electron drag has been known since the 1960s.[13,14] Recently, the extension of spin waves into the paramagnetic domain and their carrier drag capability, a.k.a. paramagnon electron drag, was reported.[3–5] Above the transition temperature, depending on the paramagnon and electron lifetimes, paramagnons may behave like magnons and contribute to the thermopower *via* a similar drag effect resulting from the s–d exchange interactions.

The prospects offered by magnons and paramagnons can have a significant impact on the progress in finding high-efficiency thermoelectric materials.[3–5,15–17] Consequently, magnetic semiconductors are getting increasing attention in the thermoelectric research community. Parallel and antiparallel alignments of the spin ensembles define the magnetic nature of the materials. Ferromagnetic (FM) and antiferromagnetic (AFM) alignments in magnetic semiconductors create two different quantized spin waves or magnons that can both drag itinerant carriers and enhance the total thermopower. Interestingly, both FM and AFM materials can have magnons and paramagnons below and above their transition temperatures, respectively.[2–5] In this regard, both FMs and AFMs can be of interest, although there is a rather fundamental difference in their MED characteristics. Despite the differences in the FM and AFM magnons, significant MED thermopowers have already been reported for both the FM and AFM materials.[2–5] Therefore, the matter of which type of magnetic ordering can lead to a larger MED thermopower is still unanswered. As we will discuss, due to the differences in their magnetic nature, a different spectrum of magnons interact with itinerant carriers in FMs and AFMS, which leads to different magnon, magnon by electron, and electron by magnon relaxation times. The changes in such

[a] Department of Materials Science and Engineering, North Carolina State University, Raleigh, NC 27606, USA. E-mail: dvashae@ncsu.edu
[b] Department of Electrical and Computer Engineering, North Carolina State University, Raleigh, NC 27606, USA
[c] School of Dentistry, Marquette University, Milwaukee, WI 53233, USA

† Electronic supplementary information (ESI) available: S1: Crystal structure of $Mn_{1-x}Cr_xSb$ from XRD analysis. S2: Spin characteristics of $Mn_{1-x}Cr_xSb$. See DOI: 10.1039/c9tc06330g

Table 1 Comparison of physical properties between MnSb and CrSb

Physical properties	MnSb	CrSb
Crystal structure	Hexagonal	Hexagonal
Magnetic nature	FM intermetallic	AFM semiconductor
Transition temperature	$T_C \approx 600$ K	$T_N \approx 713$ K
Paramagnetic Curie temperature (Θ_p)	~592 K	~−634 K
Effective moment (μ_{eff})	4.48 μ_B	4.79 μ_B
Electrical conductivity (at 300 K)	~10 000 S cm^{-1}	~8000 S cm^{-1}

relaxation times are reflected directly in the MED thermopower in these materials.

To experimentally validate the consequences of such differences and to make a fair comparison between FM and AFM MED thermopowers, we selected two very similar material systems with the only significant difference being that one is FM and the other AFM, namely MnSb and CrSb. Both materials have a NiAs hexagonal crystal structure with similar electrical conductivity and other physical properties (as listed in Table 1; refer to Fig. 5 for the electrical conductivity). However, MnSb is an FM semimetal, and CrSb is an AFM semiconductor. To make a complete comparison, we synthesized and studied a comprehensive range of compositions of $Mn_{1-x}Cr_xSb$ and characterized them to find the trend of the magnonic contribution to the thermoelectric behaviors as the material system changes from FM to AFM with the increase of Cr concentration. The obtained experimental results are found to be in good agreement with the expected trends from fundamental physical discussions. Our objective in this work is to compare the variation of the magnon drag thermopower with respect to the AFM and FM magnetic ordering experimentally. Theoretical analysis of the magnon and electron transport relevant to the magnon drag thermopower deserves further detailed studies.

Sample preparation and characterization

$Mn_{1-x}Cr_xSb$ samples with x = 0, 0.2, 0.5, 0.7, 0.8 and 1 were synthesized using 99.99% pure Mn, Sb, and Cr powders. The elemental powders for x = 0–0.8 were milled under an Ar-environment in a WC cup for 8 h at 650 rpm using a Fritsch P7PL planetary ball mill. The elemental powders for CrSb were mixed in the Spex cup for the same amount of time under an Ar-environment. The $Mn_{1-x}Cr_xSb$ (x = 0–0.8) powders were subsequently annealed at 800 °C for 24 h under vacuum to achieve a homogenous phase with approximately uniform distribution without the general phase impurity of $MnSb_2$. CrSb powder was annealed at 900 °C for 24 h. The annealed samples were crushed and milled again for 8 h. The powders were loaded into graphite dies inside an atmosphere-controlled glove box filled with Ar, and subsequently consolidated into cylindrical ingots using a spark plasma sintering (SPS) instrument located inside the same glove box. The SPS operation inside the glovebox ensured an inert atmosphere and prevented potential oxidation. For the $Mn_{1-x}Cr_xSb$ (x = 0–0.8) samples, Spark plasma sintering was performed at approximately 50 MPa pressure at a constant heating rate of 60 °C min^{-1} at a maximum temperature of around 700 °C and a soaking time of 20 min. For CrSb, SPS was performed at 900 °C with 20 min soaking time. To prevent the sticking of the CrSb sample inside the graphite die, we used a graphite foil inside the die during SPS. O_2 and H_2O levels were always kept at <0.01 ppm inside the glove box. All the consolidated ingots had >97% density of the ideal value. Different characterization methods, *i.e.*, XRD, electrical, magnetic, and thermal transport measurements, were performed on the solid samples. X-ray diffraction (XRD) patterns illustrated in Fig. 1 were collected using a Rigaku Miniflex with Cu-Kα radiation at 0.154 nm wavelength. XRD analysis shows a polycrystalline phase of $Mn_{1-x}Cr_xSb$ with no other phase impurity. No trace of Cr, Mn, Sb, MnO, $MnSb_2$, or Cr_2Sb_3 phases is observed. The positive shifts of the diffraction peaks of $Mn_{1-x}Cr_xSb$ samples towards higher angles indicate Mn substitution by Cr into the MnSb lattice. A more detailed discussion on the XRD data is given in Section S1 (ESI†).

To study the spin mediated thermoelectric transport properties of $Mn_{1-x}Cr_xSb$ samples, we performed different characterizations on the samples, including the measurement of magnetic, electrical, and thermal properties. Magnetic susceptibility as a function of temperature was measured using a Quantum Design DynaCool 12T system from 300 K to 900 K at a weak field excitation of 1000 Oe. Electrical conductivity was measured by a standard 4-point probe method using Linseis equipment under a He environment from around 300 K to 850 K. The thermopower was measured simultaneously with the same instrument. The measurement was performed for five different temperature gradients, and the thermopower was calculated from the slope fitting to five separate temperature and voltage differences. Each measurement was repeated four times and then averaged. The accuracy of the analysis was verified by inspecting the linear fit to the (ΔT–ΔV) data set. A thin disk (diameter 6 mm, thickness <0.7 mm) was cut from the cylindrical ingot to measure the thermal diffusivity in the same direction as that of the electrical conductivity and

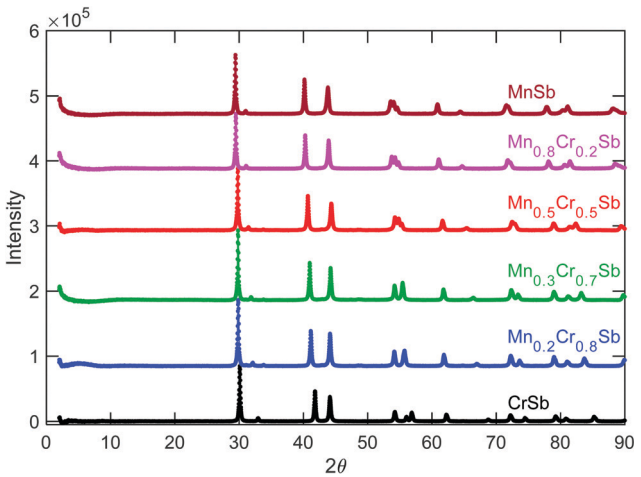

Fig. 1 XRD patterns of $Mn_{1-x}Cr_xSb$ samples (x = 0, 0.2, 0.3, 0.5, 0.8, 1).

Seebeck coefficient. The thermal diffusivity (D) was measured using a laser flash apparatus (Linseis) under vacuum from 300–900 K. The mass density (ρ) was measured using the Archimedes method. The specific heat was measured by differential scanning calorimetry (DSC) from 300 K to 900 K under N_2 flow to avoid the formation of oxide phases. The thermal conductivity (κ) was calculated using the relation $\kappa = \rho C_p D$. The electronic contribution to the thermal conductivity was estimated from the electrical conductivity using the Wiedemann–Franz law. All the characterization results are discussed in the next section in detail.

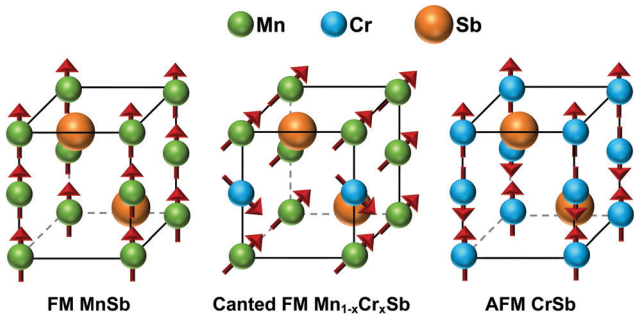

Fig. 3 Magnetic unit cell with spin alignments for MnSb, $Mn_{1-x}Cr_xSb$ ($0 < x < 1$) and CrSb.

Magnetic properties

Magnetic susceptibility as a function of temperature was measured for $Mn_{1-x}Cr_xSb$ samples to study the variation of magnetic behavior with respect to Cr substitution for Mn or *vice versa*. Both magnetic susceptibility and inverse magnetic susceptibility are illustrated in Fig. 2.

According to the magnetic moment shown in Fig. 2, MnSb is ferromagnetic with a Curie temperature of around 590 K, while CrSb is antiferromagnetic with a Néel temperature of around 700 K. During Cr substitution for Mn in MnSb, the Curie temperature shifts towards a lower temperature, and eventually, both FM and AFM phases appear in $Mn_{0.3}Cr_{0.7}Sb$ and $Mn_{0.2}Cr_{0.8}Sb$. Cr substitution at the Mn site creates a canted FM structure in the MnSb lattice (shown in Fig. 3), which causes deviation of the FM structure with an increase in Cr and finally the creation of the AFM phase.[18–22] FM and AFM phases present in $Mn_{1-x}Cr_xSb$ can be explained from the superexchange interaction *via* itinerate carriers where the optimum magnetic structure is obtained from the spin orientation dependent energy minimization during carrier hopping between two sites (Mn–Mn or Mn–Cr or Cr–Cr).[20] Despite the FM phase in MnSb, a small AFM phase appeared below around 466 K due to the stable composition of $Mn_{1+x}Sb$, which creates excess Sb in the lattice.[23] Therefore, two phase transitions occur in MnSb: AFM → FM at around 466 K and FM → PM (paramagnetic) at about 566 K.

From the magnetic susceptibility trends, a magnetic phase diagram can be made using the Curie–Weiss law: $\chi = C/(T \pm \theta_P)$, where χ is the magnetic susceptibility, θ_P is the paramagnetic Curie temperature (negative sign is used for FM, and positive sign is used for AFM), and C is the Curie constant. All the parameters extracted from the Curie–Weiss law are summarized in Table 2, which agrees with the previously published results.[20–22]

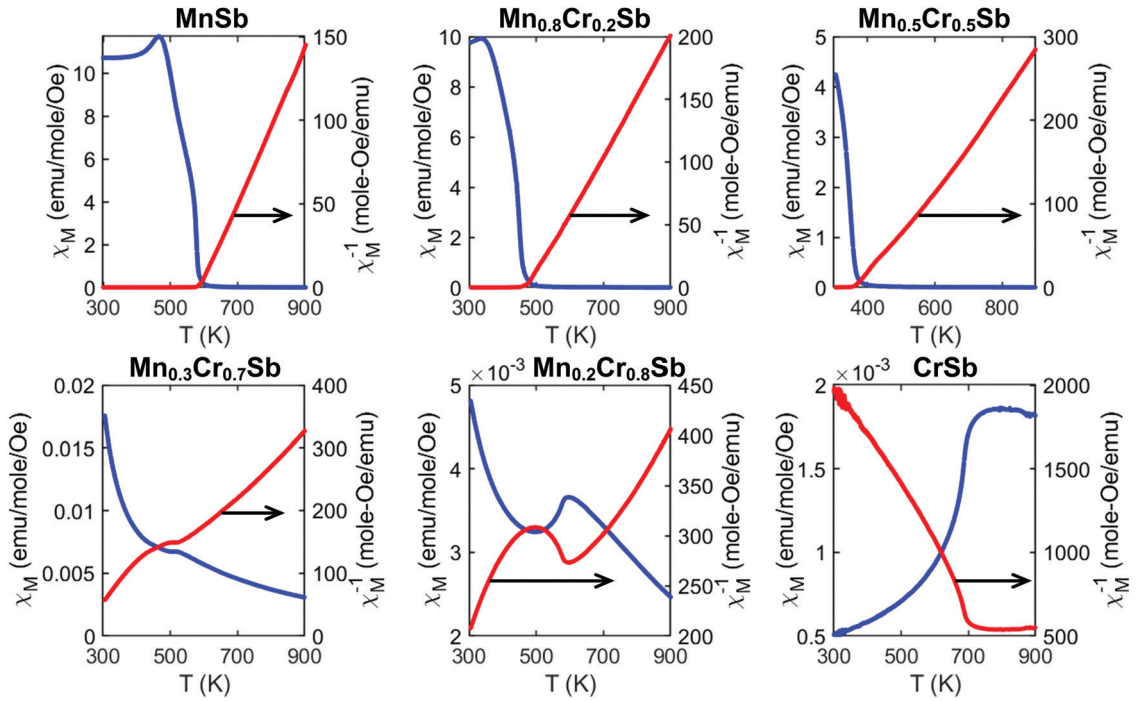

Fig. 2 Magnetic susceptibility and inverse magnetic susceptibility as a function of temperature for $Mn_{1-x}Cr_xSb$ samples under weak field excitation.

Table 2 Magnetic parameters of $Mn_{1-x}Cr_xSb$ obtained from the Curie–Weiss law

Materials	Curie temp., T_C (K)	Néel temp., T_a (K)	Paramagnetic Curie temp., θ_P (K)	Spin number, S	Curie constant, C (emu K^{-1} $mole^{-1}$)
MnSb	~600	—	592	1.64	2.18
$Mn_{0.8}Cr_{0.2}Sb$	~480	—	486	1.59	2.06
$Mn_{0.5}Cr_{0.5}Sb$	~390	—	412	1.42	1.73
$Mn_{0.3}Cr_{0.7}Sb$	~250	~520	253	1.45	1.79
$Mn_{0.2}Cr_{0.8}Sb$	~150	~600	220	1.40	1.70
CrSb	—	~710	−634	1.87	2.68

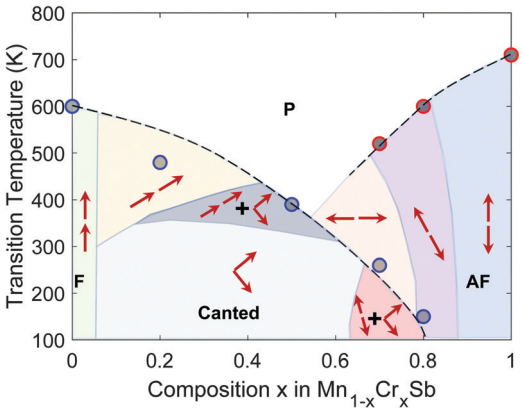

Fig. 4 Magnetic phase diagram of $Mn_{1-x}Cr_xSb$ ($x \leq 0 \leq 1$) showing the transition temperatures and the corresponding FM, canted FM, AFM, and PM regions. All the spin alignments are shown with respect to the c-axis.

The magnetic phase diagram for the $Mn_{1-x}Cr_xSb$ shown in Fig. 4, which is in agreement with the literature.[21,22] In the phase diagram, all the magnetic phases as a function of temperature are illustrated. In between FM and AFM phases, canted FM and inclined AFM phases with respect to the c-axis are also present. Details on the intermediate magnetic phases have been discussed in previous literature.[21,22] Further discussions are presented in Section S2 (ESI†).

Thermoelectric transport properties

Both magnetic and electronic structures of $Mn_{1-x}Cr_xSb$ samples play an essential role in determining their transport properties. Therefore, a summary of the electronic structure of MnSb and CrSb is discussed here. MnSb is an FM intermetallic structure, and CrSb is an AFM semiconductor. Due to the presence of point symmetry of D_{3d} in MnSb, 3d orbitals of Mn are split into a_{1g}^t, c_{1g}^t, and, e_g which is also common in all $Mn_{1-x}Cr_xSb$ samples.[21] The a_{1g}^t level is less occupied by magnetic electrons of Mn except for the presence of excess Mn in $Mn_{1+x}Sb$, where excess Mn provides electrons to the Mn–Mn bond along the [001] direction to increase the c-axis without carrying a magnetic moment.[21] Therefore, in Mn-excess MnSb, electrical conductivity becomes lower due to the smaller energy overlap caused by the lowering of a_{1g}^t due to the presence of excess electrons in the Mn–Mn bond.[21] The magnetic moment is also decreased and specific heat is increased in $Mn_{1+x}Sb$ due to the same phenomena.[21] In MnSb, hybridization occurs between Mn 3d and Sb 5p states, which lowers the magnetic moment per Mn atom (around 3.5 μ_B instead of the ideal 5 μ_B) and provides p–d interaction (an indirect exchange interaction) between Mn and free-electrons along with the direct exchange interaction due to the d–d overlap of Mn atoms along the c-axis.[24,25] The majority and minority spin states of Mn 3d have an exchange energy splitting below Tc, majority spin states of Mn 3d orbitals are filled with 5 electrons, and the minority spin states are partially filled.[24–26] As the minority spin state of Mn 3d and bonding Sb 5p contain the Fermi level,[24] the Fermi surface is hole-like with a predominant contribution from the hole surface of the Sb 5p electronic surface and a small contribution from low mobility Mn 3d electrons.[24] Therefore, the Hall coefficient of MnSb is positive due to the hole-like nature of the Fermi surface.[24,26] However, the thermopower of MnSb is negative at room temperature, which might seem contradictory. This can be explained by the higher Mn 3d electron density of states (DOS) compared to the low Sb 5p hole DOS near the Fermi level; hence, the dominant scattering of holes by minority Mn 3d spins occurs *via* the p–d interaction.[26] The thermopower is proportional to $1/e\cdot\partial \log \sigma(E)/\partial E|_{E=E_F}$, where $\sigma(E)$ is proportional to $n_h/N_d(E_F)$. n_h is the number of holes and N_d is the 3d minority electron spin DOS. With an increase of the Fermi energy, n_h remains almost unaffected; however, $N_d(E_F)$ increases rapidly due to the sharp slope of the minority d orbital DOS near the Fermi energy. Therefore, the hole scattering by minority spins becomes dominant and $\sigma(E)$ reduces. The thermopower becomes negative due to the negative $\partial \log \sigma(E)/\partial E|_{E=E_F}$.[24,26] The smaller density of states (DOS) of the holes at the Fermi level also leads to a low electronic heat capacity contribution.[24]

On the other hand, the CrSb electronic structure shows a close relation to the MnTe structure due to the similar reduction in c/a ratio.[27,28] CrSb also shows hybridization between Cr 3d orbital and Sb 5p orbitals[29] with the same energy splitting as MnSb. Despite the similarity, Mn–Mn covalent bonds and the associated exchange interactions are substituted by Cr–Cr covalent bonds. In $Mn_{1-x}Cr_xSb$ samples ($0 < x < 1$), Mn–Mn, Mn–Cr, and Cr–Cr bonds are present, which caused the modification of the electronic structure and, hence, the transport properties. But, in general, the band structure, hybridization nature, and energy state splitting are the same in all $Mn_{1-x}Cr_xSb$ samples.

From the understanding of the magnetic and electronic structure of $Mn_{1-x}Cr_xSb$ samples, transport properties, *i.e.*, electrical conductivity, thermopower, and thermal conductivity, are measured to investigate the thermoelectric trends in the $Mn_{1-x}Cr_xSb$ samples. The results are illustrated in Fig. 5. All $Mn_{1-x}Cr_xSb$

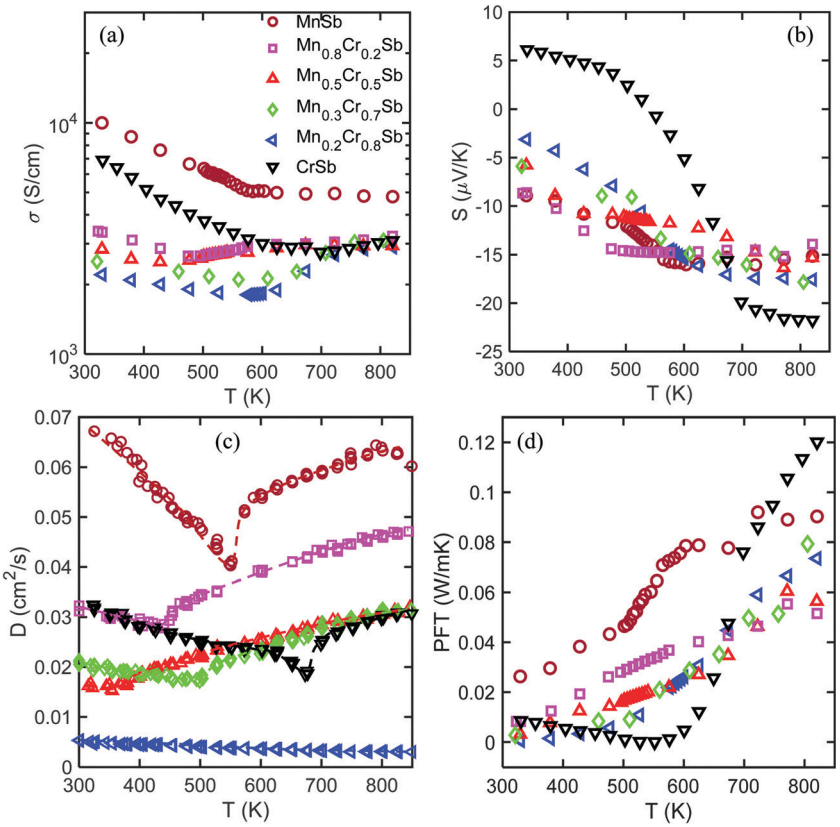

Fig. 5 Transport properties of $Mn_{1-x}Cr_xSb$ samples: (a) electrical conductivity, (b) thermopower, (c) thermal diffusivity, and (d) power factor × temperature (PFT = $S^2\sigma T$).

samples show high p-type electrical conductivity over around 2000 S cm^{-1} at 300 K, and MnSb, and CrSb have higher conductivities of about 10 000 S cm^{-1} and 8000 S cm^{-1} at 300 K, respectively. The CrSb sample has a positive thermopower at 300 K, indicating p-type conductivity. Conductivities of all the samples except $Mn_{0.2}Cr_{0.8}Sb$ and $Mn_{0.3}Cr_{0.7}Sb$ become constant after their respective transition temperatures, presumably due to the spin disorder scattering, which reaches a maximum at the corresponding transition temperatures. At higher temperatures (>750 K), the conductivity of $Mn_{1-x}Cr_xSb$ samples ($0 < x < 1$) reaches the conductivity of CrSb at that temperature. As shown in Fig. 5(b), the thermopower of $Mn_{1-x}Cr_xSb$ samples except CrSb is negative at 300 K and remains negative at a higher temperature, while the thermopower of CrSb is positive at 300 K and becomes negative at a higher temperature.

All the samples show a significant increment in thermopower, which starts before the transition temperature, reaches the maximum around the transition temperature, and then maintains the acquired excess thermopower at higher temperatures. This notable enhancement of thermopower is attributed to the magnon-carrier drag effect, while the excess thermopower kept in the paramagnetic domain is associated with the paramagnon-carrier drag effect.[3]

A variation in the advective drag thermopower with the diffusion thermopower coming from the electronic contribution is observed from the thermopower trends, which will be discussed in more detail in the later sections. Fig. 5 also demonstrates the thermal diffusivity and power factor times temperature (PFT = $S^2\sigma T$) for the $Mn_{1-x}Cr_xSb$ samples. All the samples show a distinct peak in thermal diffusivity at their corresponding magnetic transition temperatures. The peaks that appeared in thermal diffusivity can be attributed to the enthalpy of transformation required for the phase transition. The peaks in thermal diffusivity at the phase transition are also reported in previous reports.[30,31] The phase transition also caused the appearance of characteristic peaks in the heat capacity plots, which are shown in later sections. The thermal diffusivity peaks are more significant in MnSb and CrSb, while the change is smoother for the other samples. Thermal diffusivity decreases with the increase of Cr in the MnSb system. CrSb and MnSb show a higher power factor among all samples, while CrSb has the highest PFT of 0.12 W mK^{-1} at around 825 K. The thermoelectric figure-of-merit (zT) for MnSb and CrSb is approximately 0.007 and 0.017 at about 825 K, respectively.

Magnon–electron drag thermopower: FM *vs.* AFM

From the thermopower trends shown in Fig. 5, a distinct magnon-drag contribution was observed for $Mn_{1-x}Cr_xSb$ samples at around their corresponding transition temperatures. To determine and compare the different thermopower contributions from

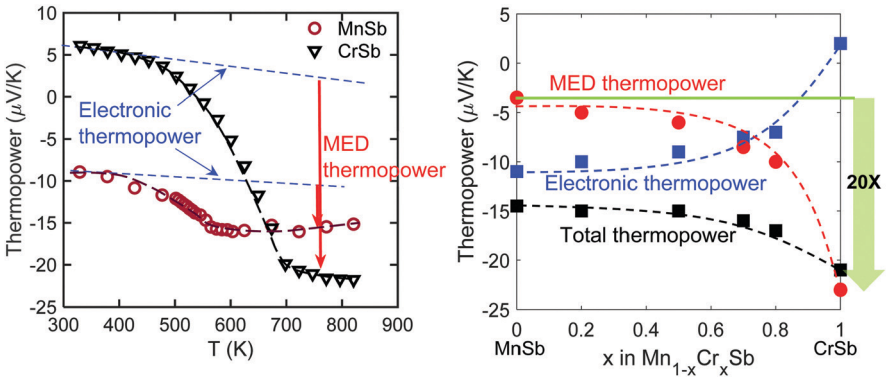

Fig. 6 Electronic thermopower and magnon–electron drag (MED) thermopower contribution to total thermopower of MnSb and CrSb (left), and the comparison of MED thermopower, electronic thermopower, and total thermopower among $Mn_{1-x}Cr_xSb$ samples.

electron and magnon, we assessed both the magnon–electron drag thermopower and electronic thermopower at 750 K from the data. For the electronic thermopower at 750 K, the linear low-temperature thermopower trends (where the magnon drag thermopower contribution is negligible) extended up to high temperature. Then, the electronic thermopower is subtracted from the total thermopower to determine the drag thermopower.[13] Fig. 6 (left) demonstrates the individual thermopower contributions from the electron thermal diffusion and magnon–electron drag (MED) for CrSb and MnSb. All the contributions, along with the total thermopower at 750 K for the $Mn_{1-x}Cr_xSb$ samples, are illustrated in Fig. 6 (right). It can be seen that in CrSb, an AFM system, the MED is approximately 20 times stronger than in MnSb, an FM system. The trends also show that MED thermopower increases with an increase of Cr content in the $Mn_{1-x}Cr_xSb$ samples, which means that MED thermopower rises with the rise in the AFM nature of the material.

This observation suggests that magnons can provide a higher drag effect on electrons in AFM compared to FM materials. As magnon–electron drag thermopower depends on both carrier relaxation time due to magnons and magnon heat capacity, the role of both parameters needs to be analyzed. From the electrical conductivity and thermopower data, both carrier concentration and mobility for MnSb and CrSb were estimated using standard transport equations.[32,33] The estimated carrier concentration at room temperature ($\sim$300 K) assuming a free carrier effective mass is around 8×10^{21} cm^{-3} and 7×10^{21} cm^{-3} for MnSb and CrSb, respectively, while the mobility at room temperature is found to be about 7 cm^2 V^{-1} s^{-1} and 6 cm^2 V^{-1} s^{-1} for MnSb and CrSb, respectively. The obtained values are within the range of previously reported values.[34,35] The estimated carrier relaxation time is, therefore, 4 fs and 3.4 fs for MnSb and CrSb, respectively. It is expected that the spin disorder scattering should be the dominant scattering mechanism near the transition temperature;[13] therefore, one may assume that these values are close to the carrier relaxation times due to magnons. The carrier lifetime in FM MnSb and AFM CrSb is in the same range.

To determine the magnon heat capacity, Cp was measured for both MnSb and CrSb within the 320–900 K temperature range, as illustrated in Fig. 7. Heat capacity data from both MnSb and CrSb

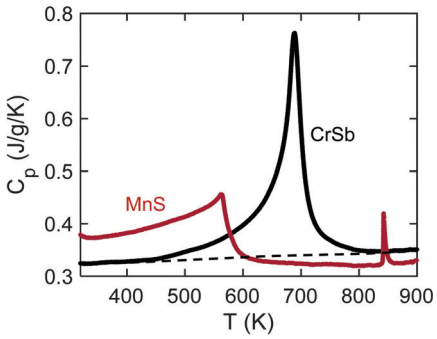

Fig. 7 Heat capacity for ferromagnetic MnSb and antiferromagnetic CrSb.

evidence a strong contribution from the magnons, shown as excess value added to the lattice heat capacity. The maximum contribution is obtained around the magnetic transition temperature. For MnSb, a new peak appears at 850 K, which corresponds to the peritectic reaction "$Mn_xSb \rightarrow Mn_xSb + Liquid$".[23] The peaks observed in heat capacity for MnSb and CrSb near the transition temperatures are caused by the enthalpy required for the phase transition. In both samples, the magnon contribution to the heat capacity (C_m) starts at a lower temperature than the transition temperature, and it decreases quickly after the transition temperature. A notable observation is that the magnon contribution to the heat capacity is about 5$\times$ stronger in CrSb than in MnSb, which should lead to a higher MED in this material. FM and AFM magnons have different characteristics due to their different dispersion relation and degeneracy, thermodynamic and transport properties, and their wavevector dependent interaction with the carriers, and different spin-dependent scattering.[36] Therefore, magnon–electron drag nature is also different in FM and AFM materials, which is discussed in more detail in the following section.

Spin-dependent scattering in FM and AFM magnon

Magnon, a quasiparticle for quantized spin waves, can act as a spin-scattering center like the magnetic ions in Kondo lattices. In a Kondo system, two kinds of spin-dependent scattering can

happen, namely, spin-flip and non-spin-flip scattering, which depend on the magnetic band structure of the magnetic ions. In a system with magnon quasiparticles, a similar kind of spin-dependent scattering can happen. In a collinear AFM material, symmetry guarantees that magnon modes are doubly degenerate, while they are non-degenerate in FMs. Therefore, if everything else is similar, MED in AFMs is expected to be twice that in FMs. Noting that MED in CrSb is twenty times larger, there must be some more effective processes involved that lead to the observed significant difference.

Magnon-drag thermopower can be expressed as:[3–5]

$$\alpha_d = \frac{k_B}{e}\frac{mc^2\,\tau_m}{k_B T \tau_{em}} \times \frac{1}{1+\tau_m/\tau_{me}}$$

where the first part is the first order magnon-drag effect, which has a magnon relaxation lifetime, τ_m (including Umklapp processes, boundary scattering, *etc.*, except the scattering by electrons), and an electron by magnon relaxation lifetime, τ_{em} (only including electron scattering by magnons). In the second-order magnon-drag term, τ_{me}, electron by magnon relaxation, is included, where only magnon scattering by electrons is considered. Similar to the case of phonon electron drag, this term, a.k.a. the saturation effect, is required to take into account the mutual interaction of electrons and magnons.[37,38]

Magnon electron scattering can involve one, two, or more magnons, which must satisfy the law of momentum conservation. Therefore, the magnon electron scattering may or may not result in the spin-flip of the itinerant carriers. As a magnon cannot provide energy to itinerate electrons, spin-flip scattering can only happen in AFM materials due to the degeneracy of the band. In FMs, due to band splitting, the itinerant electrons are unlikely to experience spin-flip scattering as the magnon cannot provide that energy (Fig. 8). Therefore, both spin-flip and non-spin-flip scattering often occur by AFM magnons, while only non-spin-flip scattering occurs in FMs up to the transition temperature. Spin-flip scattering is dominantly a one-magnon process, and it can only scatter electrons within an equi-energy surface defined by k, where k is the electron wavevector. The largest possible momentum transfer is, therefore, $2k$, assuming a spherical equi-energy surface with radius k. Hence, all scattered magnons must have a momentum $\hat{q} \leq 2\hat{k}$, where q is the magnon wavevector. Non-spin-flip scattering is generally a two magnon process, which is not bound to the mentioned wavevector condition and happens in FMs. These different spin-dependent scattering mechanisms can significantly modify the magnon (τ_m), magnon by electron (τ_{me}), and electron by magnon (τ_{em}) relaxation times, which are the critical parameters for determining the magnon-drag thermopower.

Due to the constraint on the wavevector of the AFM magnons that interact with the carriers, less magnons are involved in the determination of the magnon relaxation time, which leads to a larger τ_m than that of FM magnons where all magnon modes contribute to τ_m. Consequently, the first order MED is enhanced in AFMs compared to FMs.

The situation is different for the second-order MED. It is expected that the second-order effect should be smaller for multi-magnon scattering than for one-magnon scattering. There are mainly two reasons for this. First, as discussed, the magnon lifetime (τ_m) due to multi-magnon scattering is smaller. Second, as we will discuss, τ_{me} will be larger in multi-magnon scattering. For the case of one magnon scattering, again due to the wavelength constraint $\hat{q} \leq 2\hat{k}$, fewer magnons have to be given the same velocity as electrons in the AFM system, which leads to a smaller magnon by electron relaxation time (τ_{me}). Therefore, both the first and second-order terms are larger in AFMs than those of FMs, which eventually provides a higher drag thermopower in AFMs.

As discussed, spin-flip scattering contributes much more than non-spin flip scattering in AFM semiconductors to both

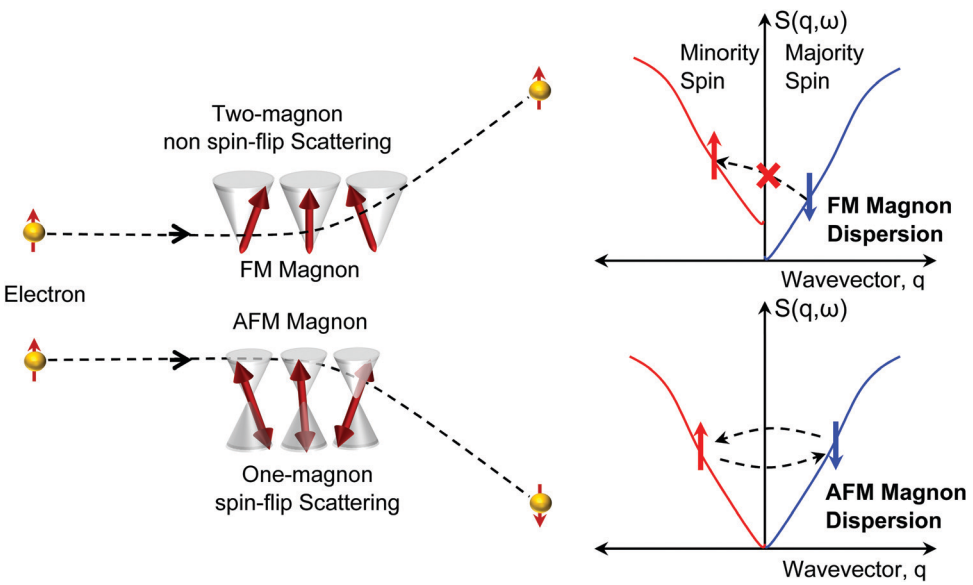

Fig. 8 Spin-dependent scattering in the FM and AFM systems and their corresponding dispersion relations.

the first and second-order drag effects. In other words, one may think of τ_{em} being primarily determined by spin-flip scattering. Therefore, unless the second-order effect is extremely large, this assumption is reasonable as long as the temperature is not much higher than T_N. At $T > T_N$, it is expected that the spin-flip and non-spin flip relaxation times are of the same order of magnitude.

At last, it should be noted that the magnon lifetime τ_m and magnon velocity c have completely different trends *versus* temperature in FMs and AFMs, which would directly affect the MED near the phase transition temperature. This is primarily because the long-wavelength fluctuation of the magnetization near the phase transition is very different for FMs and AFMs. Ferromagnetic critical fluctuations happen with long-wavelength near T_C, which has a long lifetime due to the thermodynamic slowing down.[39] Consequently, the lifetime of long-wavelength magnons becomes infinite near T_C. Moreover, in FM semiconductors, a large peak is often observed in the resistivity near T_C, which indicates that τ_{em} becomes very small. Both the effects, $\tau_m \rightarrow \infty$ and $\tau_{em} \rightarrow 0$, suggest that the first-order MED must become infinite in FMs near T_C. However, the thermodynamic slowing down of long-wavelength magnons also decreases the magnon velocity causing $c \rightarrow 0$ near T_C. Therefore, for a complete understanding of the MED in FM semiconductors, a precise calculation of τ_m, τ_{em}, and c is necessary near T_C.

In contrast, the critical fluctuations near T_N in AFMs are of a different nature. The AFM fluctuations of the magnetization, unlike those of FMs, are not long wavelength and are rather fluctuations with long wave-vector q. They correspond precisely to the AFM order.[39] This rather significant difference between the FMs and AFMs is associated directly with the magnetic susceptibility, which becomes infinite at T_C in FMs, but takes a finite value at T_N in AFMs. Consequently, there is no thermodynamic slowing down of the long-wavelength magnons in AFMs and the magnon lifetime is proportional to the inverse of the wave-vector square, *i.e.* $\tau_m \propto q^{-2}$.[40,41] For the same reason that the long-wavelength fluctuations do not show a critical trend in AFMs near the Néel temperature, the magnon velocity does not change significantly at T_N. The inelastic neutron scattering on MnTe indeed demonstrated that the magnon lifetime τ_m is not a strong function of temperature near T_N.[3]

Conclusion

Magnon electron drag and its extension to paramagnons can give a much larger thermopower than simple diffusion thermopower because magnons and paramagnons are bosonic quasi-particles, and their thermopower is independent of the number of particles. This offers great promise to enhance the thermoelectric figure-of-merit. Magnons in FMs and AFMs can produce different values of drag thermopower due to the differences in their dispersion, lifetime, and thermodynamic properties. The electronic band structure in FMs and AFMs also imposes different types of interactions between magnons and carriers, which modifies the nature of the spin-dependent scatterings. The magnon-carrier scattering in AFMs is dominated by one-magnon scattering, but in FMs, it is dominated by multi magnon scattering. This leads to significant differences in both antiferromagnetic magnon lifetime (τ_m) and magnon electron relaxation time (τ_{me}) compared to those of ferromagnets. While τ_m enhances, τ_{me} reduces in AFMs compared to FMs.

Consequently, both the first order and second order magnon electron drag thermopowers are larger in AFMs. As an experimental proof of concept, a series of $Mn_{1-x}Cr_xSb$ compounds with different x values was synthesized and studied. It was observed that AFM CrSb gives approximately 20× higher drag thermopower than that of MnSb despite their very similar other physical properties. The magnetic susceptibility, heat capacity, thermal diffusivity, and other thermoelectric transport properties of $Mn_{1-x}Cr_xSb$ were measured for different values of x and the trend of the magnon electron drag when the material changes from FM to AFM with the increase of x was studied and discussed in detail.

Conflicts of interest

There are no conflicts to declare.

Acknowledgements

The authors would like to acknowledge the funding support by the Air Force Office of Scientific Research (AFOSR) under contract number FA9550-12-1-0225 and the National Science Foundation (NSF) under grant numbers ECCS-1351533, ECCS-1515005, and ECCS-1711253.

References

1 M. V. Costache, G. Bridoux, I. Neumann and S. O. Valenzuela, Magnon-drag thermopile, *Nat. Mater.*, 2012, **11**, 199–202.
2 S. J. Watzman, R. A. Duine, Y. Tserkovnyak, S. R. Boona, H. Jin, A. Prakash, Y. Zheng and J. P. Heremans, Magnon-drag thermopower and Nernst coefficient in Fe, Co, and Ni, *Phys. Rev. B*, 2016, **94**, 144407.
3 Y. Zheng, T. Lu, Md. M. H. Polash, M. Rasoulianboroujeni, N. Liu, M. E. Manley, Y. Deng, P. J. Sun, X. L. Chen, R. P. Hermann, D. Vashaee, J. P. Heremans and H. Zhao, Paramagnon drag yields a high thermoelectric figure of merit in Li-doped MnTe, *Sci. Adv.*, 2019, **5**(9), eaat9461.
4 D. Vashaee, M. M. H. Polash, V. Perelygin, M. Rasoulianboroujeni, Y. Zheng, T. Lu, N. Liu, M. Manley, R. Hermann, A. I. Smirnov, J. P. C. Heremans and H. Zhao, Spin Effects Making zT > 1, Bulletin of the American Physical Society, March 4–8, 2019, Boston, Massachusetts.
5 D. Vashaee, M. M. H. Polash, V. Perelygin, M. Rasoulianboroujeni, Y. Zheng, T. Lu, N. Liu, M. E. Manley, R. P. Hermann, A. I. Smirnov, J. P. Heremans and H. Zhao,

Spin Effects in Paramagnetic Thermoelectric Materials Leading to zT > 1, ICT/ACT 2019, June 30–July 4, 2019, Gyeongju, Korea.
6 N. Tsujii, A. Nishide, J. Hayakawa and T. Mori, Observation of enhanced thermopower due to spin-fluctuation in weak itinerant ferromagnet, *Sci. Adv.*, 2019, **5**, eaat5935.
7 Y. Wang, N. S. Rogado, R. J. Cava and N. P. Ong, Spin entropy as the likely source of enhanced thermopower in $Na_xCo_2O_4$, *Nature*, 2003, **423**, 425–428.
8 G. Tang, F. Xu, Y. He, L. Wang, L. Qiu and Z. Wang, Evidence for giant spin entropy contribution in thermoelectric $Ca_3Co_4O_{9+\delta}$, *Phys. Status Solidi B*, 2012, **250**(7), 1327–1330.
9 W. Koshibae and S. Maekawa, Effects of Spin and Orbital Degeneracy on the Thermopower of Strongly Correlated Systems, *Phys. Rev. Lett.*, 2001, **87**(23), 236603.
10 S. R. Boona, R. C. Myers and J. P. Heremans, Spin caloritronics, *Energy Environ. Sci.*, 2014, **7**, 885–910.
11 S. T. B. Goennenwein and G. E. W. Bauer, Electron spins blow hot and cold, *Nat. Nanotechnol.*, 2012, **7**, 145–147.
12 M. E. Lucassen, C. H. Wong, R. A. Duine and Y. Tserkovnyak, Spin-transfer mechanism for magnon-drag thermopower, *Appl. Phys. Lett.*, 2011, **99**, 262506.
13 J. D. Wasscher and C. Haas, Contribution of magnon-drag to the thermoelectric power of antiferromagnetic MnTe, *Phys. Lett.*, 1964, **8**, 302–304.
14 F. J. Blatt, D. J. Flood, V. Rowe, P. A. Schroeder and J. E. Cox, Magnon-drag thermopower in iron, *Phys. Rev. Lett.*, 1967, **18**, 395.
15 B. Flebus, R. A. Duine and Y. Tserkovnyak, Landau-Lifshitz theory of the magnon-drag thermopower, *Europhys. Lett.*, 2016, **115**, 57004.
16 Y. Ren, J. Yang, Q. Jiang, D. Zhang, Z. Zhou, X. Li, J. Xin and X. He, Synergistic effect by Na doping and S substitution for high thermoelectric performance of p-type MnTe, *J. Mater. Chem. C*, 2017, **5**, 5076–5082.
17 W. Xie, S. Populoh, K. Gałązka, X. Xiao, L. Sagarna, Y. Liu, M. Trottmann, J. He and A. Weidenkaff, Thermoelectric study of crossroads material MnTe *via* sulfer doping, *J. Appl. Phys.*, 2014, **115**, 103707.
18 T. Hirone, S. Maeda, I. Tsubokawa and N. Tsuya, On the magnetic properties of the system MnSb-CrSb, *J. Phys. Soc. Jpn.*, 1956, **11**(10), 1083–1087.
19 I. Tsubokawa, Magnetic anisotropy of chromium antimonide and its manganese substitutes, *J. Phys. Soc. Jpn.*, 1961, **16**(2), 277–281.
20 W. J. Takei, D. E. Cox and G. Shirane, Magnetic structure in the MnSb-CrSb, *Phys. Rev.*, 1963, **129**(5), 2008–2018.
21 W. Reimers, E. Hellner, W. Treutman, P. J. Brown and G. Heger, Neutron diffraction studies on single crystal in the NiAs-type system MnSb-CrSb, *J. Magn. Magn. Mater.*, 1980, **15–18**, 479–480.
22 W. Reimers, E. Hellner, W. Treutman and G. Heger, Magnetic phase diagram of the system Mn1-xCrxSb ($0 \leq x \leq 1$), *J. Phys. C: Solid State Phys.*, 1982, **15**, 3597–3615.
23 G. Y. Iwamoto, C. D. A. Rodrigues, L. A. D. S. Iwamoto and R. D. A. Vieira, New Peritectoid Reaction Identified at the MnSb Alloy, *Mater. Res.*, 2019, **22**(suppl 1), e20180647.
24 R. Coehoorn, C. Hass and R. A. de Groot, Electronic structure of MnSb, *Phys. Rev. B: Condens. Matter Mater. Phys.*, 1985, **31**(4), 1980–1996.
25 R. Masrour, E. K. Hlil, M. Hamedoun, A. Benyoussef, O. Mounkachi and H. El Moussaoui, Electronic and Magnetic Properties of MnSb Compounds, *J. Supercond. Novel Magn.*, 2015, **28**, 1815–1819.
26 T. Chen, W. Stutius, J. W. Allen and G. R. Stewart, Magnetic and electric properties of MnSb, *AIP Conf. Proc.*, 1976, **29**, 532.
27 B. T. M. Willis, Crystal structure and antiferromagnetism of CrSb, *Acta Crystallogr.*, 1953, **6**, 425–426.
28 S. Polesya, G. Kuhn, S. Mankovsky, H. Ebert, M. Regus and W. Bensch, Structural and magnetic properties of CrSb compounds: NiAs structure, *J. Phys.: Condens. Matter*, 2012, **24**, 036004.
29 P. Radhakrishna and J. W. Cable, Inelastic-neutron-scattering studies of spin-wave excitations in the pnictides MnSb and CrSb, *Phys. Rev. B: Condens. Matter Mater. Phys.*, 1996, **54**(17), 11940–11943.
30 M. T. Agne, P. W. Voorhees and G. J. Snyder, Phase Transformation Contributions to Heat Capacity and Impact on Thermal Diffusivity, Thermal Conductivity, and Thermoelectric Performance, *Adv. Mater.*, 2019, **31**(35), 1902980.
31 D. R. Brown, T. Day, K. A. Borup, S. Christensen, B. B. Iversen and G. J. Snyder, Phase transition enhanced thermoelectric figure-of-merit in copper chalcogenides, *APL Mater.*, 2013, **1**, 052107.
32 S. Walia, S. Balendhran, H. Nili, S. Zhuiykov, G. Rosengarten, Q. H. Wang, M. Bhaskaran, S. Sriram, M. S. Strano and K. Kalantar-zadeh, Transition metal oxides – Thermoelectric-properties, *Prog. Mater. Sci.*, 2013, **58**(8), 1443–1489.
33 K. Vandaele, S. J. Watzman, B. Flebus, A. Prakash, Y. Zheng, S. R. Boona and J. P. Heremans, Thermal spin transport and energy conversion, *Mater. Today Phys.*, 2017, **1**, 39–49.
34 M. Nogami, M. Sekinobu and H. Doi, Hall effect in Manganese Antimonide, *Jpn. J. Appl. Phys.*, 1964, **3**(10), 572–575.
35 M. Regus, G. Kuhn, S. Mankovsky, H. Ebert and W. Bensch, Investigations of the crystallization mechanism of CrSb and CrSb2 multilayered films using in-situ X-ray diffraction and in-situ X-ray reflectometry, *J. Solid State Chem.*, 2012, **196**, 100–109.
36 B. Y. Pan, T. Y. Guan, X. C. Hong, S. Y. Zhou, X. Qiu, H. Zhang and S. Y. Li, Specific heat and thermal conductivity of ferromagnetic magnons in Yttrium Iron Garnet, *Europhys. Lett.*, 2013, **103**(3), 37005.
37 E. H. Sondheirner, The Kelvin relations in thermoelectricity, *Proc. R. Soc. London, Ser. A*, 1956, **234**(1198), 391.
38 C. Herring, Theory of the thermoelectric power of semiconductors, *Phys. Rev.*, 1954, **96**(5), 1163–1187.
39 P. G. de Gennes, *Magnetism*, ed. G. T. Rado and H. Suhl, Academic Press. Inc., New York, 1963, vol. 3, p. 115.
40 P. G. de Gennes, Inelastic magnetic scattering of neutrons at high temperatures, *J. Phys. Chem. Solids*, 1958, **4**(3), 223–226.
41 H. Mori and K. Kawasaki, Theory of Dynamical Behaviors of Ferromagnetic Spins, *Prog. Theor. Phys.*, 1962, **27**(3), 529–570.